HHS Public Access

Author manuscript

J Nanopart Res. Author manuscript; available in PMC 2023 March 17.

Published in final edited form as:

J Nanopart Res. 2014 January ; 16(1): . doi:10.1007/s11051-013-2078-3.

Single-walled carbon nanohorns decorated with semiconductor quantum dots to evaluate intracellular transport

Kristen A. Zimmermann,
School of Biomedical Engineering and Sciences, Virginia Polytechnic Institute and State University, ICTAS Building, Stanger Street, Blacksburg, VA 24061, USA

David L. Inglefield Jr,
Department of Chemistry, Virginia Polytechnic Institute and State University, ICTAS II Building, Washington Street, Blacksburg, VA 24061, USA

Jianfei Zhang,
Department of Chemistry, Virginia Polytechnic Institute and State University, Hahn Hall South Building, Blacksburg, VA 24061, USA

Harry C. Dorn,
Department of Chemistry, Virginia Tech Carilion Research Institute, 2 Riverside Circle, Roanoke, VA 24016, USA

Timothy E. Long,
Department of Chemistry, Virginia Polytechnic Institute and State University, Hahn Hall South Building, Blacksburg, VA 24061, USA

Christopher G. Rylander,
School of Biomedical Engineering and Sciences, Virginia Polytechnic Institute and State University, ICTAS Building, Stanger Street, Blacksburg, VA 24061, USA

Department of Mechanical Engineering, Virginia Polytechnic Institute and State University, ICTAS Building, Stanger Street, Blacksburg, VA 24061, USA

M. Nichole Rylander
School of Biomedical Engineering and Sciences, Virginia Polytechnic Institute and State University, ICTAS Building, Stanger Street, Blacksburg, VA 24061, USA

Department of Mechanical Engineering, Virginia Polytechnic Institute and State University, ICTAS Building, Stanger Street, Blacksburg, VA 24061, USA

Kristen A. Zimmermann: kazimmer@vt.edu

Abstract

Single-walled carbon nanohorns (SWNHs) have great potential to enhance thermal and chemotherapeutic drug efficiencies for cancer therapies. Despite their diverse capabilities, minimal research has been conducted so far to study nanoparticle intracellular transport, which is an

Correspondence to: Kristen A. Zimmermann, kazimmer@vt.edu.

Electronic supplementary material The online version of this article (http://dx.doi.org/10.1007/s11051-013-2078-3) contains supplementary material, which is available to authorized users.

important step in designing efficient therapies. SWNHs, like many other carbon nanomaterials, do not have inherent fluorescence properties making intracellular transport information difficult to obtain. The goals of this project were to (1) develop a simple reaction scheme to decorate the exohedral surface of SWNHs with fluorescent quantum dots (QDs) and improve conjugate stability, and (2) evaluate SWNH–QD conjugate cellular uptake kinetics and localization in various cancer cell lines of differing origins and morphologies. In this study, SWNHs were conjugated to CdSe/ZnS core/shell QDs using a unique approach to carbodiimide chemistry. Transmission electron microscopy and electron dispersive spectroscopy verified the conjugation of SWNHs and QDs. Cellular uptake kinetics and efficiency were characterized in three malignant cell lines: U-87 MG (glioblastoma), MDA-MB-231 (breast cancer), and AY-27 (bladder transitional cell carcinoma) using flow cytometry. Cellular distribution was verified by confocal microscopy, and cytotoxicity was also evaluated using an alamarBlue assay. Results indicate that cellular uptake kinetics and efficiency are highly dependent on cell type, highlighting the significance of studying nanoparticle transport at the cellular level. Nanoparticle intracellular transport investigations may provide information to optimize treatment parameters (e.g., SWNH concentration, treatment time, etc.) depending on tumor etiology.

Keywords

Single-walled carbon nanohorn (SWNH); Quantum dot (QD); Cellular distribution; Uptake kinetics; Cancer; Nanobiotechnology

Introduction

Carbonaceous nanomaterials (CNMs) have impacted the engineering community significantly over the recent decades for various applications, such as hydrogen storage (Lee and Lee 2000; Dillon et al. 1997; Schlapbach and Zuttel 2001), sensors (e.g., gas, temperature, biomolecules, etc.; Suehiro et al. 2003; Dorozhkin et al. 2005; Liu et al. 2008; Wang et al. 2004), and medical diagnostics and treatments (Bianco et al. 2008; Endo et al. 2008; Al Faraj et al. 2009), because of their excellent mechanical, chemical, and thermal properties. The versatile characteristics of these materials arise from the ability to manipulate and control their sizes, shapes, and surface functionalities. Within the medical field, CNMs have been studied widely to enhance cancer treatment and diagnostic techniques, such as drug delivery systems (Dhar et al. 2008; Bhirde et al. 2009; Muralkami et al. 2004; Xu et al. 2008), photoabsorbers in laser-based therapies (Burke et al. 2009; Whitney et al. 2011; Fisher et al. 2010), and magnetic resonance imaging (MRI) contrast agent carriers (Dorn et al. 2010; Miyawaki et al. 2006; Al Faraj et al. 2009; Richard et al. 2008). The strong carbon–carbon bonds present in CNMs create chemically and mechanically inert carriers. Chemotherapeutic and MRI contrast agents are thus protected from degradation as they are transported to the sites of interest (Ajima et al. 2005), in addition to potentially reducing the systemic toxicity of the chemotherapeutic agents. Cancer is the second leading cause of death in the United States, and advancements such as the use of nanomaterials in the diagnosis and treatment of the disease are imperative to reduce this ranking (Siegel et al. 2012).

Single-walled carbon nanohorns (SWNHs) share similar structures to the more conventional carbon nanotubes (CNTs); however, in the case of SWNHs, the single graphene sheets are rolled into conical, rather than tubular shapes. Strong van der Waals forces between the open ends of individual SWNHs cause them to assemble into a larger spherical aggregate (Yudasaka et al. 1999). The spherical structures can take the form of dahlias, buds, and seeds as described by Yudasaka et al. (2008). Dahlia SWNHs are the most promising because they can be synthesized with extreme purity in large quantities and were, therefore, selected for this study. SWNHs are appealing for their biomedical applications in relation to other forms of CNMs for numerous reasons. The most significant advantage is the elimination of metal catalysts during synthesis, thereby reducing cytotoxic effects (Bianco et al. 2008; Yudasaka et al. 2008). Furthermore, nanoparticle shape and size are proven to greatly affect nanoparticle's intravenous transport, intratumoral transport, and intracellular transport. Chithrani et al. (2006) found that spherical gold nanoparticles of 50-nm diameter were endocytosed more readily than gold nanorods of various aspect ratios. SWNHs are thus predicted to have a shape that requires less energy to be endocytosed than high aspect ratio CNTs. Finally, SWNHs have larger surface areas and internal storage spaces than CNTs for enhanced exohedral surface modification (e.g., receptor-targeting moieties, chemotherapeutic drugs, coatings for biocompatibility, etc.) and endohedral drug loading, rendering them more attractive for active drug delivery systems (Utsumi et al. 2005).

Nanomaterials will encounter a series of transport barriers before reaching the site of interest, whether targeting the bulk tumor tissue or individual cellular compartments (Jain and Stylianopoulos 2010; Li et al. 2012). Nanoparticle design (e.g., shape, size, material, and surface characteristics) will influence transport through the pathways previously stated (Decuzzi et al. 2010; Li et al. 2012). The study of "nano-biotransport" is fundamental to the success of nanotechnology to insure the delivery of adequate concentrations of chemotherapy and other adjuvant agents, such as photoabsorptive materials, photodynamic therapy agents, and radiosensitizers. In addition, information specifically regarding intracellular transport will have implications in directing agents to the appropriate cellular pathways. Potential cytotoxicity or long-term effects of endocytosed nanoparticles may also correlate to transport information, such as the intracellular location of the particles or the uptake kinetics (Teeguarden et al. 2007).

Many nanomaterials, such as iron oxide nanoparticles and CNMs (with the exception of a portion of single-walled CNTs), lack fluorescent properties sufficient to monitor their optical transport in vitro or in vivo, limiting the study of their transport (Miyawaki et al. 2009). Therefore, more invasive and laborious techniques are necessary, such as paraffin embedding and sectioning of samples to monitor transport at discrete time points with electron microscopy (EM). In addition, low contrast between CNMs and cell or organelle membranes makes techniques such as EM difficult (Porter et al. 2007). Even though gadolinium has been incorporated into SWNHs to enhance contrast in studying SWNH biodistribution using EM (Miyawaki et al. 2009), few attempts have been made to optically track SWNH transport. This study focuses on developing fluorescently tagged SWNH conjugates to study intracellular transport in vitro using semiconductor quantum dots (QDs).

Traditionally, many organic fluorescent probes, such as fluorescein and cyanines, are used to enhance imaging of nanoparticles in biomedical research (Zhang et al. 2008); however, the use of QDs has generated significant interest because they have several benefits over conventional probes. The most prominent advantages are that they are resistant to both photo- and chemical degradation over time and they have a wide excitation band with a narrow emission band. Furthermore, they are brighter than other fluorophores and can be tuned to emit specific wavelengths by altering the diameter of the crystal (Susumu et al. 2009; Resch-Genger et al. 2008). In particular, near-infrared (NIR) emission wavelengths can be achieved to overcome attenuation problems when used in vivo. The current standard nanocrystal composition is cadmium selenide (CdSe), which generates a concern of toxicity when used in biology due to Cd ions leaching from the nanocrystal. Many studies aim to determine in vitro and in vivo toxicity; however, the results are ambiguous and highly dependent on nanocrystal size, surface charge, stability in solution, and physical environment (Derfus et al. 2004; Hoshino et al. 2004; Geys et al. 2008; Gao et al. 2004). Recent research is directed in the synthesis of Cd-free nanocrystals, though their commercial availability is limited and the quantum yield has yet to reach that of CdSe nanocrystals (except in the NIR emission region; Li et al. 2009; Yong et al. 2009; Zimmer et al. 2006). Despite these concerns, QDs can be easily surface modified with target ligands, polymers, or chemotherapeutic agents.

Previous groups have demonstrated that QDs can be successfully conjugated to CNT surfaces with various noncovalent (Raffaelle et al. 2006) or covalent methods, including acid-chloride (Haremza et al. 2002), carbodiimide (Ozkan et al. 2003; Wong and Banerjee 2002; Guo et al. 2008), in situ QD growth (Feng et al. 2009; Wang et al. 2009), and streptavidin adsorption (Bottini et al. 2006). Nevertheless, limited study has been conducted to conjugate QDs to SWNHs (Dorn et al. 2010). Each of these methods has challenges, such as the use of harsh solvents during synthesis, lack of stability (i.e., precipitation), cost, and the likelihood that QDs will detach from the CNT surface. This study builds upon the carbodiimide approach used by Dorn et al. (2010) to optimize the method and improve conjugate stability. Previous studies using this technique typically conjugate amine-functionalized QDs, often prepared with monothiols, to carboxyl-functionalized CNTs. However, these methods may not be stable because of the labile interaction between monothiols and QDs (Medintz et al. 2005). The combination of carbon nanohorns and other inorganic nanoparticles, such as QDs may have substantial impact in fields outside of biological imaging. These heterostructures could create new opportunities as supercapacitors, gas, vapor, or molecular sensors, field emission displays, etc. (Li et al. 2011).

In this study, SWNHs were successfully conjugated to semiconductor QDs using a conventional carbodiimide approach. We hypothesized that thiol-functionalized SWNHs will serve as multidentate substrates to interact with the QD surfaces and enhance conjugation stability, thereby creating a highly decorated SWNH with surface conjugated QDs. SWNH–QD materials characterization was performed, and intracellular transport of SWNHs decorated with QDs was evaluated herein by flow cytometry and confocal microscopy using three cell lines: AY-27, MDA-MB-231, and U-87 MG. These three cell lines were selected to evaluate variations in cellular uptake kinetics (i.e., the rate with which nanoparticles are

internalized over time) and uptake efficiency (i.e., the amount of nanoparticles internalized over time) as a result of different cellular morphologies and cancer origination. This study highlights the importance of studying the dynamic transport of nanoparticles in multiple cell lines to better predict nanoparticle–cell interactions. This is the first in-depth study of SWNH–QD conjugation to conceptualize SWNH transport in vitro. The goals of this study were: (1) to develop a simple reaction scheme for exohedral conjugation of fluorescent QDs to SWNHs and (2) to evaluate SWNH–QD conjugate cellular uptake kinetics and efficiency in various cancer cell lines of differing origins and morphologies in vitro.

Materials and methods

Materials

SWNHs were synthesized by colleagues at Oak Ridge National Laboratories (Oak Ridge, TN) using a laser vaporization technique based on previously published methods (Puretzky et al. 2008). The SWNHs used in this study were approximately 80–100 nm in diameter, as determined by transmission EM (TEM) and ImageJ (data not shown). CdSe/zinc sulfide core/shell QD powder (emission peak at 630 nm) was purchased from Ocean Nanotech, LLC (Springdale, AR). Chloroform and phosphate buffered saline (PBS) mixture were purchased from Fisher Scientific (Pittsburgh, PA). 1-Ethyl-3-(3-dimethylaminopropyl) carbodiimide (EDC), *N*-hydroxysulfosuccinimide (NHS), 2-aminoethanethiol (AET), and fetal bovine serum (FBS) were purchased from Sigma-Aldrich (St. Louis, MO). 1,2-Distearoyl-*sn*-glycero-3-phosphoethanolamine-*N*-[methoxy(polyethylene glycol)-2000] (ammonium salt), DSPE-PEG (MW = 2,805.54) was purchased from Avanti Polar Lipids (Alabaster, AL). Durapore® 0.2 μm nylon membrane filters were purchased from Millipore (Billerica, MA). Dulbecco's Modified Eagle's Medium: Nutrient Mixture F-12 (DMEM/F-12), Roswell Park Memorial Institute (RPMI) 1640 medium, penicillin–streptomycin (pen–strep), and 0.25 % trypsin were purchased from Invitrogen (Carlsbad, CA). Eagle's Minimum Essential Medium (EMEM) was purchased from American Type Culture Collection (ATCC; Manassas, VA).TEM lacey carbon coated copper grids and lacey carbon/carbon film coated copper grids were purchased from Electron Microscopy Sciences (Hatfield, PA) and Pacific Grid Tech (San Francisco, CA), respectively.

Single-walled nanohorn oxidation

Water dispersible SWNHs were created by acid functionalization (Fig. 1). Similar procedures have been shown to produce oxygen containing functional groups that are negatively charged and are extremely useful for further chemical modification (Chen et al. 2001; Tchoul et al. 2007). In brief, approximately 300 mg of pristine SWNHs were sonicated in 50 mL of 8.0 M nitric acid (HNO_3) for 1 h (0.5–0.6 w/v%). The reaction vessel was then placed in an oil bath, heated to 120 °C, and stirred for 24 h under reflux. Upon completion, SWNHs were filtered with a 0.1 μm-pore hydrophilic PVDF membrane and rinsed with deionized water until the filtrate reached a pH of 7.0. SWNHs were removed from the membrane and sonicated in 50 mL of 1 M HCl for 1 h. The SWNH–HCl suspension was stirred for 24 h at room temperature to insure the complete conversion of carboxylate anions to fully protonated carboxylic acid groups. The product was filtered

again and washed with deionized water until a pH of 7.0 was reached. The oxidized SWNHs (SWNHox) were then dried in a vacuum oven for 36–48 h.

Carbon nanohorn–QD conjugation

SWNHox were dispersed in sterile deionized water at a final concentration of approximately 0.1 mg/mL by sonication. The dispersion of SWNHox was added to a reaction vessel containing 0.1 M EDC and stirred briefly, followed by the addition of 5 mM NHS. The thiol-containing compound, AET, was then added to the flask at a concentration of 0.2 M and the pH of the solution was adjusted to approximately 6.0 by drop wise addition of 1.0 M HCl to optimize the carbodiimide reaction and prevent disulfide formation. The solution was stirred vigorously overnight at room temperature. AET was selected for this conjugation scheme because of its small size, leading to minimal steric effects. The final product is thiol-functionalized SWNHs (SWNH-SH).

After 24 h, as-purchased QD powder was dissolved in chloroform to a concentration of 1.0 mg/mL and added to the SWNH-SH in a weight ratio of 4:1 QD to SWNH. The ratio of QD to SWNH can be altered to control the degree of QD conjugation to the exohedral surface. The pH of the solution was adjusted to approximately 7.0 by drop wise addition of 1.0 M NaOH to enhance particle stability. The as-purchased QD powders contain octadecylamine surface-stabilizing ligands, in which the amine has an affinity to the heavy metals, Zn or Cd. Monothiols, such as AET, have higher affinity for heavy metals than the amines, causing a covalent ligand interchange process on the QD surface at the solvent phase interface. The high affinity of thiol for Cd and Zn causes QDs to move from the organic (chloroform) phase into the aqueous (SWNH-SH in deionized water) phase, creating a SWNH–QD complex dispersed in deionized water. A schematic summarizing the conjugation process is depicted in Fig. 1.

SWNH–QDs suspended in deionized water were separated from the chloroform phase with a separatory funnel. The product was then filtered with a 0.2-μm-pore hydrophilic nylon membrane and washed four times with sterile deionized water to remove any residual reagents and unreacted QDs. After four washes, the 630-nm emission peak of the filtrate was diminished, suggesting all unbound QDs were removed. To sterilize the particles before in vitro use, SWNH–QDs were filtered with 70 % ethanol, followed by four subsequent sterile deionized water washes. SWNH–QDs trapped on the filter membrane were then sonicated off of the membrane for 1 min in a 0.5 mg/mL DSPE-PEG aqueous solution. This suspension was then stirred for 1 h at room temperature (SWNH–QD + PEG). PEG is commonly used to enhance dispersibility and prevent opsonization of serum proteins in biological environments (Klibanov et al. 1991). A concentration of 0.5 mg/mL DSPE-PEG was selected because it showed minimal toxicity in MDA-MB-231 cells using an alamarBlue assay over 24 h, while significantly improving SWNH–QD dispersibility (Supplementary Information [SI], Fig. S1). However, higher concentrations of DSPE-PEG (greater than 1.0 mg/mL) did prove to reduce cellular metabolism. Sterile, deionized water was used to make a stock suspension of SWNH–QDs to eliminate the risk of serum protein adhesion during the 1 h of mixing. SWNH–QD + PEG was diluted with the respective cell culture medium to the concentrations of interest. Photographs of each step were taken under

ultraviolet (UV) excitation to visually demonstrate QD conjugation (Fig. 3b, d). Henceforth, the final product, SWNH–QD + PEG, will be referred to as SWNH–QD.

Materials characterization

SWNH–QD conjugation was characterized with TEM using either a Zeiss 10CA TEM equipped with AMT Advantage GR/HR-B CCD camera system (Carl Zeiss AG; Oberkochen, Germany) or an FEI™ Titan 300 equipped with high spatial resolution electron dispersive spectroscopy, EDS (FEI; Hillsboro, OR) for high-resolution imaging and elemental quantification. Elemental analysis of SWNH–QD conjugates was performed with EDS to confirm the presence of QD elements (i.e., Cd, Se, and Zn) and linker elements (i.e., N and S). Accelerating voltages of 100 and 300 kV were used to obtain TEM images, respectively, with each instrument. The complexes were further characterized by dynamic light scattering (DLS) and electrophoretic light scattering (ELS) using a Zetasizer NanoZS system (Malvern Instruments; Worcestershire, UK) to obtain their hydrodynamic radius and zeta potential (ζ). DLS and ELS were performed at 25 °C in water with attenuator position, count rate, and number of runs set to automatic. A 632.8-nm HeNe laser with vertically polarized light was used as the light source. A concentration of 0.05 mg/mL SWNH–QD in water was used for both measurements. DLS and spectrophotometry were performed using 10 × 10 mm quartz cuvettes, and ELS was performed using disposable zeta cells (Malvern Instruments; Worcestershire, UK). SWNH–QDs were further characterized with UV–Vis and fluorescence (FL) spectroscopy using a SpectraMAX M2^{e} microplate reader (Molecular Devices; Sunnyvale, CA). Samples were excited with a wavelength of 488 nm to simulate the laser light used for in vitro experiments.

Cell culture

The cells in this study include human mammary gland adenocarcinoma epithelial-derived cells, MDA-MB-231 (ATCC); human glioblastoma epithelial-derived cells, U-87MG(ATCC); and *N*-(4-[5-nitro-2-furyl]-2-thiazolyl)formamide-induced rat bladder transitional cell carcinoma cells, AY-27, originally developed by Dr. S. Selman and Dr. J. Hampton (Medical College of Ohio, Toledo, Ohio) and kindly donated by Dr. John Robertson (Virginia Tech, Blacksburg, VA). MDA-MB-231, U-87 MG, and AY-27 cells were cultured in complete DMEM/F-12, EMEM, and RPMI 1640 medium, respectively—each supplemented with 10 % FBS and 1 % pen–strep and maintained in a humidified atmosphere at 37 °C, 5 % CO_2, and 95 % air.

Cytotoxicity evaluation

In vitro cytotoxicity was evaluated by measuring the metabolic activity using alamarBlue, according to manufacturers' protocol (AbD Serotec; Raleigh, NC). SWNH–QDtoxicity at a concentration of 0.025 mg/mL was analyzed after 3- and 24-h incubation. For this assay, 25,000 cells per well were seeded in tissue culture-treated polystyrene (TCPS) 48-well dishes and were incubated for 48 h (~90 % confluent), changing the media after every 24 h. Cells were rinsed with PBS and treated with 500 μL of SWNH–QD ($n = 3$) for 3 or 24 h. Cells were then rinsed four times with ice-cold PBS to halt endocytosis processes and remove excess SWNH–QDs. Next, 500 μL of 10 % alamarBlue® in media was added to each sample and incubated for 3 or 24 h. Then, 100 μL aliquots from each sample were

taken in triplicate and placed into a 96-well dish, totaling nine readings per experimental group. Absorbance was measured using a SpectraMAX M2^e microplate reader (Molecular Devices; Sunnyvale, CA) at 570 and 600 nm according to the manufacturer's protocol. Each experimental group ($n = 3$) was tested and analyzed independently. The results were represented as the mean value ± sample standard deviation. Significance of results was verified with Student's t test, and a 95 or 99 % confidence was used to determine statistical significance between groups.

Flow cytometry cellular binding/uptake

FL-activated cell sorting (FACS), a specific type of flow cytometry, was used to estimate cellular uptake rates of SWNH–QDs into three different cancer cell lines. In the context of this study, cellular uptake will refer to both nonspecific cellular surface binding and internalization, as they cannot be differentiated with the FACS instrument used. Cells were seeded in TCPS 12-well dishes at 100,000 cells per well for each time point and incubated for 48 h before treatment (~90 % confluent), changing the medium every 24 h. A 0.1 mg/mL stock suspension of SWNH–QDs and 0.5 mg/mL DSPE-PEG in sterile deionized water was prepared. The SWNH–QD solution was diluted with the respective cell culture medium to a concentration of 0.025 mg/mL and sonicated for 30 s immediately before experiments. This concentration was used to efficiently visualize uptake kinetics over time. Cell culture medium was aspirated, and cells were rinsed once with PBS. One milliliter of SWNH–QD was added to each well and incubated for 0, 5, 15, 30, 45, 60, 120, and 180 min. After treatment, cells were rinsed four times with ice-cold PBS by gentle rocking to halt any endocytosis processes and remove any unbound SWNH–QDs. Cells were then trypsinized with 100 μL of 0.25 % trypsin–EDTA for 3–5 min. Fresh media (1 mL) was added to each well, and cell suspensions were transferred to centrifuge tubes, followed by centrifugation at 150×g for 5 min at 4 °C. Media supernatant was aspirated, and 150 μL of fresh media was added to each group creating a final cell density of 1×10^6 cells/mL. Cell suspensions were placed on ice until analysis. The cell suspensions were analyzed using a BD Biosciences FACSARIA cell sorter (San Jose, CA). A 488-nm excitation source was used using a 610/20-nm emission filter equipped with a 595-nm-long pass filter. This experiment was performed on three separate days to obtain an average cellular uptake rate ($n = 1$) for each cell line on each day. A small sample size was used to reduce the chance of human error when handling large numbers of samples. Cellular debris was excluded with a forward versus side scatter gate, and aggregates were excluded using height and width parameters on both forward and side scatters.

Confocal microscopy

Immunofluorescent staining with confocal microscopy was performed to study the cellular distribution of SWNH–QDs. Circular glass coverslips (18-mm diameter, no. 1) were sterilized in 70 % ethanol for 15 min and placed in the bottom of each well of 12-well dishes. Cells were seeded and treated following the same conditions as for cellular uptake experiments analyzed with FACS. Cellular distributions at 0 min, 60 min, and 24 h were characterized. Following ice-cold PBS washes, cells were fixed with a 3.7 % paraformaldehyde solution for 15 min. Cells were then rehydrated with PBS; their membranes were permeabilized with a 0.5 % Triton-X solution for 15 min; and they were

subsequently blocked with 1 % BSA for 30 min. Approximately 30 nM Oregon Green® 488 Phalloidin (Invitrogen; Grand Island, NY) in PBS, an F-actinselective probe conjugated to 2′,7′-difluorofluorescein, was incubated with the cells at room temperature in the dark for 20 min. Cells were then incubated with NucBlue® Fixed Cell Stain (Invitrogen; Grand Island, NY), a room temperature-stable DAPI formulation, for 5 min and then rinsed with PBS. Vetashield Mounting Medium (Vector Laboratories; Burlingame, CA) was added to preserve the FL, and coverslips were placed on microscope slides for imaging. A Zeiss LSM510 confocal microscope (Carl Zeiss AG; Oberkochen, Germany) equipped with Enterprise UV 364 nm, Argon 488-nm, and HeNe 543-nm laser excitation sources was used for imaging.

Results

Materials' characterization

CdSe/ZnS core/shell QDs were successfully conjugated to the exohedral surface of SWNHs using a thiol-containing compound as a linker. This synthesis procedure yielded highly decorated SWNHs as evidenced by the TEM micrographs in Fig. 2a, b. The HRTEM micrograph clearly depicts successful conjugation of the two particles with high-contrast QDs attached to the exohedral surface of the low contrast SWNHs. To confirm the elemental composition of the complexes, EDS was performed on an area represented by the red circle in Fig. 2b. The high counts of Cd and carbon (C) in Fig. 2c are important in verifying the presence of QDs and SWNHs, respectively. The presence of sulfur (S) suggests successful covalent coupling between the particles via the AET linker compound. A copper (Cu) peak was attributed to the Cu TEM grid. A control experiment was performed by mixing pure SWNHs and unfunctionalized QDs. The nanoparticles were mixed in the same ratio (4:1 weight ratio of QDs to SWNHs) in chloroform. TEM micrographs (SI, Fig. S2) show minimal adhesion of QDs on the SWNH surfaces in this control experiment, further confirming covalent attachment of QDs using this method.

SWNHox, SWNH–QD, and as-purchased QDs were further characterized using UV–Vis and FL spectroscopy. The spectra were normalized to the maximum intensity for each spectrum for comparison. The UV–Vis spectrum of SWNH–QD has qualities characteristic to both SWNHox and QD samples as shown in Fig. 3a. For example, the conjugate sample is highly absorptive below 500 nm because both SWNHox and QDs also increase absorption at these wavelengths. In addition, the conjugate sample has absorbance peaks at approximately 485 and 630 nm, representing the same peaks observed for QDs alone. A slight blue-shift in FL was observed for SWNH–QD conjugates compared to QDs alone (Fig. 3c), which could be due to variations in solvent dielectric constants. Furthermore, the conjugates also have a mild fluorescent signal outside of the peak because of SWNH background FL (Fig. 3c, d), which was also observed by Zhu et al. (2011).

DLS and ELS were then performed to further characterize the size (hydrodynamic diameter) and stability (ζ) of SWNHox and SWNH–QDs (Fig. 4). DLS analysis of SWNHox and SWNH–QD dispersed in water at a concentration of 0.05 mg/mL indicated that the calculated *Z*-average hydrodynamic diameters were approximately 150 and 207 nm, respectively, averaged over five samples. The average diameter of unfunctionalized SWNHs

used in this study was in the range of 80–100 nm according to TEM analysis. ζ was then analyzed to provide a measure of suspension stability after QD conjugation. The ζ, as determined by ELS, decreased from approximately −50 to −30 mV with QD conjugation, suggesting that many of the carboxyl, hydroxyl, or other oxygen-containing groups contributing to the large electric potential of SWNHox are being used to form the amide bond with AET. The *Z*-average hydrodynamic diameter and ζ results for five samples were averaged and are summarized in Table 1 below.

Cytotoxicity analysis

Before in vitro implementation, cytotoxicity was evaluated in three cell lines using a concentration of 0.025 mg/mL. This concentration was also used for cellular uptake kinetics and efficiencies in the following studies. Cytotoxicity analysis after 3- and 24-h incubations using an alamarBlue® assay confirmed minimal toxicity in all three cell lines. Evaluation of metabolic activity showed a statistically significant increase in metabolic activity compared to the control in the AY-27 and U-87 MG cell lines after 3-h incubation. After 24-h incubation, only a statistically significant decrease in metabolic activity for the MDA-MB-231 cell line was observed (Fig. 5). Current in vitro toxicology assays are typically insufficient for determining the toxicity of nanomaterials due to discrepancies between assays; therefore, further investigation is necessary to confirm toxicity.

Cellular binding/uptake

Nonspecific cellular uptake and binding of SWNH–QD conjugates overa duration of 3 h were evaluated with flow cytometry. For the purpose of this study, cellular uptake will be defined as both internalization and nonspecific binding to the cell surfaces as it cannot be differentiated by means of the available flow cytometry system. Cellular uptake rate was quantified by the percentage of cells containing SWNH–QDs and measuring the median FL intensity at each time point (i.e., 0, 5, 15, 30, 45, 60, 120, and 180 min). In vitro research investigating the use of nanomaterials as medical tools often fails to evaluate the efficacy over various cell lines. Therefore, in this study, three different malignant cell lines were analyzed to determine if the uptake rates varied with the cell morphology. Flow cytometry data show a cell-type-dependent cellular uptake of SWNH–QDs, as shown in Fig. 6. U-87 MG, human malignant glioblastoma cells, showed the greatest SWNH–QD uptake in the least amount of time compared with MDA-MB-231, human breast cancer cells, and AY-27, rat transitional cell bladder carcinoma cells. After 60 min, approximately 95, 80, and 50 % of U-87 MG, MDA-MB-231, and AY-27 cells were sorted as positive for containing SWNH–QDs by FACS, respectively. All cells continued to uptake SWNH–QDs over time in a linear fashion according to the median FL intensity and the side-scattering information (SI, Fig. S5). Side scattering can be used as a metric of cellular uptake because it is a measure of cellular internal complexity. As the side scattering increases, the internal complexity of the cell also increases, suggesting more nanoparticle internalization. Deviations in FACS data may be due to variations in cell metabolism between passages and variations between SWNH and QD batches.

Intracellular distribution

Immunofluorescent staining was performed and imaged with confocal microscopy to analyze SWNH–QD cellular distribution. Cellular nuclei and F-actin were stained to monitor morphology and to determine the localization of SWNH–QDs. F-actin was selected to determine SWNH–QD surface binding in preference to internalization because the former interacted extensively with the cellular membrane and it provided a clearer visualization than SWNH–QD internalization. Ultimately, SWNH–QDs were found on the cell surface, as well as internalized into the cytoplasm and nuclei of all cell lines within 60 min as shown in Figs. 7, 8, and 9(b, d, all). Even after 24 h, cells continued to internalize SWNH–QD conjugates. In addition, the number of SWNH–QD conjugates found in the nuclei of all three cell lines also increased after 24 h. According to immunofluorescent staining, morphology changed minimally in all the three cell lines over a 24-h treatment with SWNH–QDs, further confirming minimal toxicity at a concentration of 0.025 mg/mL.

Interestingly, nanoparticles are known to aggregate in cell culture medium over time, reaching sizes of a few microns (Raja et al. 2007). Although particles of these sizes are typically not internalized, aggregates were found inside U-87 MG and MDA-MB-231 cells after 24 h, but not after 60 min (Figs. 8, 9). Another study by dos Santos et al. (2011) revealed a similar finding suggesting that nano- and even micron particles are internalized by nonphagocytic cell types suggesting that abnormal endocytosis processes occur in the presence of nanomaterials. This abnormal endocytosis process may be attributed to alterations in cytoskeletal stiffness following internalization.

Discussion

Although other groups have investigated various procedures for conjugating QDs to single-walled and multiwalled CNTs (SWNT, MWNT), this is one of the first studies to characterize covalent attachment of QDs to SWNHs (Dorn et al. 2010; Feng et al. 2009; Guo et al. 2008; Wong and Banerjee 2002; Ozkan et al. 2003; Raffaelle et al. 2006; Haremza et al. 2002). The carbodiimide method of conjugation used herein is not a new method for nanomaterial surface modification (Ozkan et al. 2003; Wong and Banerjee 2002; Richard et al. 2008); however, the novelty originates from developing a multidentate nanoparticle system for attachment of QDs using short linker molecules. This approach improves the interaction between SWNHs and QDs enhancing long-term stability. Previous studies with SWNTs have focused on conjugating carboxyl-functionalized tubes to amine-functionalized QDs (Haremza et al. 2002; Shi et al. 2007). In those studies, QDs were either purchased as amine-functionalized QDs or as a QD powder with organic capping ligands. Each method has its drawbacks, with the prefunctionalized QDs being costly and possessing large diameters (upward of ~40 nm), and the QD powder requiring a ligand interchange. In this study, QD powder was selected to minimize the size of the nanoparticle complexes. Traditionally, monothiols are used as capping ligands for QD surface modification; however, it has been shown that the thiol–ZnS interaction is labile (Parak et al. 2003). When coupling QDs to nanoparticles for biomedical applications, it is important to consider such details because QD detachment is not preferable while monitoring transport.

Medintz et al. (2005) described that the use of polydentate-thiolated ligands (i.e., di-thiols) may improve stability. However, these di-thiols are typically carboxylic acids, such as dihydrolipoic acid derivatives, requiring their dispersion solutions to have a basic pH. SWNHs in this study were thiol functionalized to serve as a multidentate substrate using a short linker molecule to preserve the small particle size. When SWNH–QDs were left in solution for 5 days, TEM images showed that SWNH–QDs which were synthesized using this multidentate approach (Fig. 1) remained conjugated after 5 days (SI, Fig. S4A). However, within this timeframe, QDs detached from the SWNH surface when QDs were first functionalized with the monothiol compound (AET), followed by conjugation to carboxyl-functionalized SWNHs via carbodiimide chemistry (SI, Figs. S3, S4).

To further characterize this novel approach to covalent coupling, HRTEM and EDS analyses confirmed the conjugation of QDs to the exohedral surface of SWNHs. The EDS spectra showed the presence of Cd, Zn, and Se, indicating the high-contrast particles were QDs, in addition to S and N. These results suggest that the AET linker compound has covalently coupled the two particles. SWNH–QD complexes were further characterized with UV–Vis and FL spectroscopy. The spectra of the complexes exhibited traits characteristic of both SWNHs and QDs. The FL spectra of the complexes compared to the spectra of QDs alone showed ~5-nm blue-shift in FL emission. This shift could have been caused by either successful binding of thiol groups on the SWNHs (Wuister et al. 2003; Woelfle and Claus 2007) or different dielectric constants of the solvents used in each particle suspension (SWNH–QDs were suspended in water, and QDs alone were suspended in chloroform). However, Wuister et al. (2003) performed a QD ligand interchange with hexanethiol in chloroform which resulted in a similar shift as that produced with AET in water, suggesting that the shift observed after conjugation is indeed due to the ligand interchange. Although each additional modification to the SWNH surface caused an approximate 50-nm increase in diameter, the nanoparticle size remained in the ideal range for delivery based on the enhanced permeability and retention effect (Maruyama 2011; Yuan et al. 1995). ζ of a suspension is the measurement of electric potential between the particle and solution and is, therefore, often used as a measure of particle stability in solution. After conjugation with QDs (SWNH–QD), the ζ increased 20 mV compared to SWNHox, due to the decrease in free carboxyl groups to interact with the hydrophilic environment or the neutrality of the PEG-DSPE coating. Although an increase in ζ occurred following conjugation (more positive), the final complex ζ remains within the stable range—$\zeta < -15$ or $>+15$ mV (White et al. 2007).

Cytotoxicity analysis measured with an alamarBlue® assay revealed no metabolic decrease after 3 h in all three cell lines or 24 h in the AY-27 or U-87 MG cell lines. A significant metabolic decrease was observed after 24 h for the MDA-MB-231 cell line (Fig. 5). This decrease in metabolic activity may be characteristic of initial nanoparticle–cell interactions within the specific cell line. One study showed CNMs induced a toxic response after 24 h, but a repair process appeared after 48-h incubation (Grabinski et al. 2007). Therefore, this may be an artifact of short viability time studies. This apparent toxicity may also be attributed the internalization of large SWNH–QD aggregates over the 24-h period, which may disrupt processes involved in metabolism or cell growth rate. A similar phenomenon was described by Raja et al. (2007) in the case of single-walled CNTs incubated with

smooth muscle cells. The increase in metabolic activity compared to nontreated controls observed in each cell line is most likely an artifact of CNM interference with the assay. Many standard assays currently used to evaluate toxicity cause enhanced reduction of the indicator, indicator adhesion to nanoparticles, or nanoparticle interference in absorbance or FL measurements (Monteiro-Riviere et al. 2009).

Visualizing carbon nanohorn transport was achieved through successful conjugation of CdSe/ZnS core/shell QDs. Estimation of cellular uptake rate was determined with flow cytometry. The percentage of cells containing SWNH–QD conjugates and median FL intensity per cell was used to estimate and compare the uptake rates in the three malignant cell lines. Although much research has been done to study the uptake mechanisms, intracellular localization, and specificity of nanoparticles with various properties, these interactions remain poorly understood because of variability from group to group (Kam et al. 2006; Kostarelos et al. 2007; Porter et al. 2009). It is evident that the uptake efficiency and kinetics of SWNH–QDs are highly dependent on the cell type and may affect the delivery of the nanoparticle conjugates in vivo depending on the tumor type. U-87 MG cells exhibited the highest uptake rate, followed by the MDA-MB-231 and AY-27 cell lines, respectively (SI, Table S1). These findings are supported by dos Santos et al., where cellular uptake and localization of PS nanoparticles of various sizes were studied in multiple (phagocytic and nonphagocytic) cell lines (Whitney et al. 2011). Further investigation is necessary to determine the uptake mechanisms and discrepancies between cellular uptake kinetics and efficiency. The U-87 MG cell line is highly infiltrative with its F-actin spreading across a larger area, followed by the MDA-MB-231 cell lines, and AY-27 cells, respectively. As a result, a larger surface area of the U-87 MG cells are exposed for enhanced cellular uptake compared with the other two lines. In addition, the doubling time and metabolic activity of each cell type may contribute to differences in SWNH–QD uptake rates; i.e., if a greater cell population grows during the 48-h plating time, then there will be a lower particle-to-cell ratio.

Cellular distribution observed with confocal microscopy verified the presence of surface-bound and internalized SWNH–QDs. After 60-min incubation, SWNH–QDs were primarily localized to the surface cytoplasm in all cell lines, with a few localized to the nuclei. After 24-h incubation, SWNH–QDs entered more readily into both the cytoplasm and the nuclei. In addition, SWNH–QDs began to aggregate after 24 h, and despite the large sizes of the aggregates (few microns), the cells were still able to internalize them.

Although SWNH–QD transport was not evaluated in real-time for this study, QD photostability allows them to be continuously monitored without the risk of photobleaching. This is advantageous for implementation in 3D in vitro culture systems or in vivo. While Cd-containing QDs have many deleterious effects if not coated properly (Derfus et al. 2004; Hardman 2006), they were used to develop an effective conjugation scheme because of their high-quantum yield compared to Cd-free QDs at visible wavelengths and commercial availability. However, the availability of Cd-free QDs, such as indium phosphide QDs, is growing rapidly and could replace CdSe/ZnS core/shell QDs for in vivo uses in the future.

Conclusion

SWNH–QD complexes were synthesized and characterized using thiol-functionalized SWNHs as a multidentate substrate, which improved conjugation stability compared to previous methods. This stable, covalent conjugation of QDs to SWNHs will permit the study of SWNH transport in vivo with confidence that QDs are not detaching from the SWNH surfaces. Nonphagocytic cells were shown to endocytose SWNH–QDs at substantial rates that were greatly dependent on cell type. Further investigation is necessary to determine if each cell type uses the same endocytosis process or if there is another reason for the variability. These findings support the need for thorough cell–nanoparticle interactions before clinical implementation. The localization of SWNH–QDs within the cytoplasm and nuclei has significant potential for SWNH carriers as drug delivery systems. However, ligand- or antibody-targeting strategies should be employed in the future to improve the nonspecific binding to reduce endocytosis in nonmalignant cell lines. Advancements in studying SWNH transport in real-time will enhance the development of SWNH-based cancer therapies, such as laser-induced hyperthermia and chemotherapeutic drug delivery.

Supplementary Material

Refer to Web version on PubMed Central for supplementary material.

Acknowledgments

The authors would like to thank Dr. David Geohegan at Oak Ridge National Laboratories for generously providing the SWNHs for this research; Dr. Mitsu Murayama and Jay Tuggle at Virginia Tech for assistance with TEM; Melissa Makris at Virginia Tech for her assistance with running the FACSARIA flow cytometer; and Dr. Olga Ivanova for their helpful discussions with this project. Funding for this study was provided by the National Science Foundation Early CAREER Award CBET 0955072, the National Institute of Health Grant 1R21 CA135230-01, an Institute for Critical Technology and Applied Sciences (ICTAS, Virginia Tech) Grant, the National Institute of Health Grant R21 CA156078, the National Science Foundation Grant CBET 0933571, and the National Science Foundation Graduate Research Fellowship Program.

References

Ajima K, Yudasaka M, Murakami T, Maigne A, Shiba K, Ijima S. Carbon nanohorns as anticancer drug carriers. Mol Pharm. 2005; 2 (6) 475–480. [PubMed: 16323954]

Al Faraj A, Cieslar K, Lacroix G, Gaillard S, Canot-Soulas E, Cremillieux Y. In vivo imaging of carbon nanotube biodistribution using magnetic resonance imaging. Nano Lett. 2009; 9 (3) 1023–1027. [PubMed: 19199447]

Bhirde AA, Patel V, Gavard J, Zhang GF, Sousa AA, Masedunskas A, Leapman RD, Weigert R, Gutkind JS, Rusling JF. Targeted killing of cancer cells in vivo and in vitro with EGF-directed carbon nanotube-based drug delivery. ACS Nano. 2009; 3 (2) 307–316. [PubMed: 19236065]

Bianco A, Kostarelos K, Prato M. Opportunities and challenges of carbon-based nanomaterials for cancer therapy. Expert Opin Drug Deliv. 2008; 5 (3) 331–342. [PubMed: 18318654]

Bottini M, Cerignoli F, Dawson MI, Magrini A, Rosato N, Mustelin T. Full-length single-walled carbon nanotubes decorated with streptavidin-conjugated quantum dots as multivalent intracellular fluorescent nanoprobes. Biomacromolecules. 2006; 7 (8) 2259–2263. [PubMed: 16903668]

Burke A, Ding X, Singh R, Kraft RA, Levi-Polyachenko N, Rylander MN, Szot C, Buchanan C, Whitney J, Fisher J, Hatcher HC, D'Agostino R Jr, Kock ND, Ajayan PM, Carroll DL, Akman S, Torti FM, Torti SV. Long-term survival following a single treatment of kidney tumors with multiwalled carbon nanotubes and near-infrared radiation. Proc Natl Acad Sci USA. 2009; 106 (31) 12897–12902. [PubMed: 19620717]

Chen J, Rao AM, Lyuksyutov S, Itkis ME, Hamon MA, Hu H, Cohn RW, Eklund PC, Colbert DT, Smalley RE, Haddon RC. Dissolution of full-length single-walled carbon nanotubes. J Phys Chem B. 2001; 105 (13) 2525–2528.

Chithrani BD, Ghazani AA, Chan WCW. Determining the size and shape dependence of gold nanoparticle uptake into mammalian cells. Nano Lett. 2006; 6 (4) 662–668. [PubMed: 16608261]

Decuzzi P, Godin B, Tanaka T, Lee SY, Chiappini C, Liu X, Ferrari M. Size and shape effects in the biodistribution of intravascularly injected particles. J Control Release. 2010; 141 (3) 320–327. [PubMed: 19874859]

Derfus AM, Chan WCW, Bhatia SN. Probing the cytotoxicity of semiconductor quantum dots. Nano Lett. 2004; 4 (1) 11–18. [PubMed: 28890669]

Dhar S, Liu Z, Thomale J, Dai HJ, Lippard SJ. Targeted single-wall carbon nanotube-mediated Pt(IV) prodrug delivery using folate as a homing device. J Am Chem Soc. 2008; 130 (34) 11467–11476. [PubMed: 18661990]

Dillon AC, Jones KM, Bekkedahl TA, Kiang CH, Bethune DS, Heben MJ. Storage of hydrogen in single-walled carbon nanotubes. Nature. 1997; 386 (6623) 377–379.

Dorn HC, Zhang JF, Ge JC, Shultz MD, Chung EN, Singh G, Shu CY, Fatouros PP, Henderson SC, Corwin FD, Geohegan DB, Puretzky AA, Rouleau CM, More K, Rylander C, Rylander MN, Gibson HW. In vitro and in vivo studies of single-walled carbon nanohorns with encapsulated metallofullerenes and exohedrally functionalized quantum dots. Nano Lett. 2010; 10 (8) 2843–2848. [PubMed: 20698597]

Dorozhkin PS, Tovstonog SV, Golberg D, Zhan JH, Ishikawa Y, Shiozawa M, Nakanishi H, Nakata K, Bando Y. A liquid-Ga-filled carbon nanotube: a miniaturized temperature sensor and electrical switch. Small. 2005; 1 (11) 1088–1093. [PubMed: 17193401]

dos Santos T, Varela J, Lynch I, Salvati A, Dawson KA. Quantitative assessment of the comparative nanoparticle-uptake efficiency of a range of cell lines. Small. 2011; 7 (23) 3341–3349. [PubMed: 22009913]

Endo, M, Strano, MS, Ajayan, PM. Topics in applied physics: carbon nanotubes. Vol. 111. Berlin: Springer; 2008. Potential applications of carbon nanotubes.

Feng GD, Fei Q, Xiao DH, Zhang ZQ, Huan YF. A novel silica-coated multiwall carbon nanotube with CdTe quantum dots nanocomposite. Spectrochim Acta A. 2009; 74 (2) 597–601.

Fisher JW, Sarkar S, Buchanan CF, Szot CS, Whitney J, Hatcher HC, Torti SV, Rylander CG, Rylander MN. Photo-thermal response of human and murine cancer cells to multiwalled carbon nanotubes after laser irradiation. Cancer Res. 2010; 70 (23) 9855–9864. [PubMed: 21098701]

Gao XH, Cui YY, Levenson RM, Chung LWK, Nie SM. In vivo cancer targeting and imaging with semiconductor quantum dots. Nat Biotechnol. 2004; 22 (8) 969–976. [PubMed: 15258594]

Geys J, Nemmar A, Verbeken E, Smolders E, Ratoi M, Hoylaerts MF, Nemery B, Hoet PHM. Acute toxicity and prothrombotic effects of quantum dots: impact of surface charge. Environ Health Perspect. 2008; 116 (12) 1607–1613. [PubMed: 19079709]

Grabinski C, Hussain S, Lafdi K, Braydich-Stolle L, Schlager J. Effect of particle dimension on biocompatibility of carbon nanomaterials. Carbon. 2007; 45 (14) 2828–2835.

Guo Y, Shi DL, Cho HS, Dong ZY, Kulkarni A, Pauletti GM, Wang W, Lian J, Liu W, Ren L, Zhang QQ, Liu GK, Huth C, Wang LM, Ewing RC. In vivo imaging and drug storage by quantum-dot-conjugated carbon nanotubes. Adv Funct Mater. 2008; 18 (17) 2489–2497.

Hardman R. A toxicologic review of quantum dots: toxicity depends on physicochemical and environmental factors. Environ Health Perspect. 2006; 114 (2) 165–172. [PubMed: 16451849]

Haremza JM, Hahn MA, Krauss TD. Attachment of single CdSe nanocrystals to individual single-walled carbon nanotubes. Nano Lett. 2002; 2 (11) 1253–1258.

Hoshino A, Fujioka K, Oku T, Suga M, Sasaki YF, Ohta T, Yasuhara M, Suzuki K, Yamamoto K. Physicochemical properties and cellular toxicity of nanocrystal quantum dots depend on their surface modification. Nano Lett. 2004; 4 (11) 2163–2169.

Jain RK, Stylianopoulos T. Delivering nanomedicine to solid tumors. Nat Rev Clin Oncol. 2010; 7 (11) 653–664. [PubMed: 20838415]

Kam NWS, Liu ZA, Dai HJ. Carbon nanotubes as intracellular transporters for proteins and DNA: an investigation of the uptake mechanism and pathway. Angew Chem Int Ed. 2006; 45 (4) 577–581.

Klibanov AL, Maruyama K, Beckerleg AM, Torchilin VP, Huang L. Activity of amphipathic poly(ethylene glycol) 5000 to prolong the circulation time of liposomes depends on the liposome size and is unfavorable for immunoliposome binding to target. Biochim Biophys Acta. 1991; 1062 (2) 142–148. [PubMed: 2004104]

Kostarelos K, Lacerda L, Pastorin G, Wu W, Wieckowski S, Luangsivilay J, Godefroy S, Pantarotto D, Briand JP, Muller S, Prato M, Bianco A. Cellular uptake of functionalized carbon nanotubes is independent of functional group and cell type. Nat Nanotechnol. 2007; 2 (2) 108–113. [PubMed: 18654229]

Lee SM, Lee YH. Hydrogen storage in single-walled carbon nanotubes. Appl Phys Lett. 2000; 76 (20) 2877–2879.

Li L, Daou TJ, Texier I, Tran TKC, Nguyen QL, Reiss P. Highly luminescent $CuInS_{(2)}$/ZnS core/shell nanocrystals: cadmium-free quantum dots for in vivo imaging. Chem Mater. 2009; 21 (12) 2422–2429.

Li XL, Qin YJ, Picraux ST, Guo ZX. Noncovalent assembly of carbon nanotube-inorganic hybrids. J Mater Chem. 2011; 21 (21) 7527–7547.

Li Y, Wang J, Wientjes MG, Au JL. Delivery of nanomedicines to extracellular and intracellular compartments of a solid tumor. Adv Drug Deliv Rev. 2012; 64 (1) 29–39. [PubMed: 21569804]

Liu X, Shi L, Niu W, Li H, Xu G. Amperometric glucose biosensor based on single-walled carbon nanohorns. Biosens Bioelectron. 2008; 23 (12) 1887–1890. [PubMed: 18387291]

Maruyama K. Intracellular targeting delivery of liposomal drugs to solid tumors based on EPR effects. Adv Drug Deliv Rev. 2011; 63 (3) 161–169. [PubMed: 20869415]

Medintz IL, Uyeda HT, Goldman ER, Mattoussi H. Quantum dot bioconjugates for imaging, labelling and sensing. Nat Mater. 2005; 4 (6) 435–446. [PubMed: 15928695]

Miyawaki J, Yudasaka M, Imai H, Yorimitsu H, Isobe H, Nakamura E, Iijima S. In vivo magnetic resonance imaging of single-walled carbon nanohorns by labeling with magnetite nanoparticles. Adv Mater. 2006; 18 (8) 1010–1014.

Miyawaki J, Matsumura S, Yuge R, Murakami T, Sato S, Tonnida A, Tsuruo T, Ichihashi T, Fujinami T, Irie H, Tsuchida K, Iijima S, Shiba K, Yudasaka M. Biodistribution and ultrastructural localization of single-walled carbon nanohorns determined in vivo with embedded Gd_2O_3 labels. ACS Nano. 2009; 3 (6) 1399–1406. [PubMed: 19480401]

Monteiro-Riviere NA, Inman AO, Zhang LW. Limitations and relative utility of screening assays to assess engineered nanoparticle toxicity in a human cell line. Toxicol Appl Pharmacol. 2009; 234 (2) 222–235. [PubMed: 18983864]

Muralkami T, Ajima K, Miyawaki J, Yudasaka M, Iijima S, Shiba K. Drug-loaded carbon nanohorns: adsorption and release of dexamethasone in vitro. Mol Pharm. 2004; 1 (6) 399–405. [PubMed: 16028351]

Ozkan CS, Ravindran S, Chaudhary S, Colburn B, Ozkan M. Covalent coupling of quantum dots to multiwalled carbon nanotubes for electronic device applications. Nano Lett. 2003; 3 (4) 447–453.

Parak WJ, Gerion D, Pellegrino T, Zanchet D, Micheel C, Williams SC, Boudreau R, Le Gros MA, Larabell CA, Alivisatos AP. Biological applications of colloidal nanocrystals. Nanotechnology. 2003; 14 (7) R15–R27.

Porter AE, Gass M, Muller K, Skepper JN, Midgley PA, Welland M. Direct imaging of single-walled carbon nanotubes in cells. Nat Nanotechnol. 2007; 2 (11) 713–717. [PubMed: 18654411]

Porter AE, Gass M, Bendall JS, Muller K, Goode A, Skepper JN, Midgley PA, Welland M. Uptake of noncytotoxic acid-treated single-walled carbon nanotubes into the cytoplasm of human macrophage cells. ACS Nano. 2009; 3 (6) 1485–1492. [PubMed: 19459622]

Puretzky AA, Styers-Barnett DJ, Rouleau CM, Hu H, Zhao B, Ivanov IN, Geohegan DB. Cumulative and continuous laser vaporization synthesis of single wall carbon nanotubes and nanohorns. Appl Phys A. 2008; 93 (4) 849–855.

Raffaelle RP, Landi BJ, Evans CM, Worman JJ, Castro SL, Bailey SG. Noncovalent attachment of CdSe quantum dots to single wall carbon nanotubes. Mater Lett. 2006; 60 (29–30) 3502–3506.

Raja PMV, Connolley J, Ganesan GP, Ci LJ, Ajayan PM, Nalamasu O, Thompson DM. Impact of carbon nanotube exposure, dosage and aggregation on smooth muscle cells. Toxicol Lett. 2007; 169 (1) 51–63. [PubMed: 17275220]

Resch-Genger U, Grabolle M, Cavaliere-Jaricot S, Nitschke R, Nann T. Quantum dots versus organic dyes as fluorescent labels. Nat Methods. 2008; 5 (9) 763–775. [PubMed: 18756197]

Richard C, Doan BT, Beloeil JC, Bessodes M, Toth E, Scherman D. Noncovalent functionalization of carbon nanotubes with amphiphilic Gd^{3+} chelates: toward powerful T-1 and T-2 MRI contrast agents. Nano Lett. 2008; 8 (1) 232–236. [PubMed: 18088153]

Schlapbach L, Zuttel A. Hydrogen-storage materials for mobile applications. Nature. 2001; 414 (6861) 353–358. [PubMed: 11713542]

Shi DL, Guo Y, Dong ZY, Lian J, Wang W, Liu G, Wang LM, Ewing RC. Quantum-dot-activated luminescent carbon nanotubes via a nano scale surface functionalization for in vivo imaging. Adv Mater. 2007; 19 (8) 4033.

Siegel R, Naishadham D, Jemal A. Cancer statistics. CA Cancer J Clin. 2012; 62 (1) 10–29. [PubMed: 22237781]

Suehiro J, Zhou GB, Hara M. Fabrication of a carbon nanotube-based gas sensor using dielectrophoresis and its application for ammonia detection by impedance spectroscopy. J Phys D. 2003; 36 (21) L109–L114.

Susumu, K, Medintz, IL, Mattoussi, H. Colloidal quantum dots: synthesis, photophysical properties, and biofunctionalization strategies. In: Mattoussi, H, Cheon, J, editors. Inorganic nanoprobes for biological sensing and imaging. Norwood: Artech House, Inc.; 2009. 1–26.

Tchoul MN, Ford WT, Lolli G, Resasco DE, Arepalli S. Effect of mild nitric acid oxidation on dispersability, size, and structure of single-walled carbon nanotubes. Chem Mater. 2007; 19 (23) 5765–5772.

Teeguarden JG, Hinderliter PM, Orr G, Thrall BD, Pounds JG. Particokinetics in vitro: dosimetry considerations for in vitro nanoparticle toxicity assessments. Toxicol Sci. 2007; 95 (2) 300–312. [PubMed: 17098817]

Utsumi S, Miyawaki J, Tanaka H, Hattori Y, Itoi T, Ichikuni N, Kanoh H, Yudasaka M, Iijima S, Kaneko K. Opening mechanism of internal nanoporosity of single-wall carbon nanohorn. J Phys Chem B. 2005; 109 (30) 14319–14324. [PubMed: 16852800]

Wang J, Liu GD, Jan MR. Ultrasensitive electrical bio-sensing of proteins and DNA: carbon-nanotube derived amplification of the recognition and transduction events. J Am Chem Soc. 2004; 126 (10) 3010–3011. [PubMed: 15012105]

Wang L, Niu MG, Wu ZW. In situ growth of CdSe/CdS quantum dots inside and outside of MWCNTs. Curr Appl Phys. 2009; 9 (5) 1112–1116.

White B, Banerjee S, O'Brien S, Turro NJ, Herman IP. Zeta-potential measurements of surfactant-wrapped individual single-walled carbon nanotubes. J Phys Chem C. 2007; 111 (37) 13684–13690.

Whitney JR, Sarkar S, Zhang JF, Thao D, Young T, Manson MK, Campbell TA, Puretzky AA, Rouleau CM, More KL, Geohegan DB, Rylander CG, Dorn HC, Rylander MN. Single walled carbon nanohorns as photothermal cancer agents. Laser Surg Med. 2011; 43 (1) 43–51.

Woelfle C, Claus RO. Transparent and flexible quantum dot–polymer composites using an ionic liquid as compatible polymerization medium. Nanotechnology. 2007; 18 (2)

Wong SS, Banerjee S. Synthesis and characterization of carbon nanotube–nanocrystal heterostructures. Nano Lett. 2002; 2 (3) 195–200.

Wuister SF, Swart I, van Driel F, Hickey SG, Donega CD. Highly luminescent water-soluble CdTe quantum dots. Nano Lett. 2003; 3 (4) 503–507.

Xu JX, Yudasaka M, Kouraba S, Sekido M, Yamamoto Y, Iijima S. Single wall carbon nanohorn as a drug carrier for controlled release. Chem Phys Lett. 2008; 461 (4–6) 189–192.

Yong KT, Ding H, Roy I, Law WC, Bergey EJ, Maitra A, Prasad PN. Imaging pancreatic cancer using bioconjugated InP quantum dots. ACS Nano. 2009; 3 (3) 502–510. [PubMed: 19243145]

Yuan F, Dellian M, Fukumura D, Leunig M, Berk DA, Torchilin VP, Jain RK. Vascular-permeability in a human tumor xenograft—molecular-size dependence and cutoff size. Cancer Res. 1995; 55 (17) 3752–3756. [PubMed: 7641188]

Yudasaka M, Iijima S, Yamada R, Bandow S, Suenaga K, Kokai F, Takahashi K. Nano-aggregates of single-walled graphitic carbon nano-horns. Chem Phys Lett. 1999; 309 (3–4) 165–170.

Yudasaka M, Iijima S, Crespi VH. Single-wall carbon nanohorns and nanocones. Top Appl Phys. 2008; 111: 605–629.

Zhang M, Murakami T, Ajima K, Tsuchida K, Sandanayaka ASD, Ito O, Iijima S, Yudasaka M. Fabrication of ZnPc/protein nanohorns for double photodynamic and hyperthermic cancer phototherapy. Proc Natl Acad Sci USA. 2008; 105 (39) 14773–14778. [PubMed: 18815374]

Zhu S, Han S, Zhang L, Parveen S, Xu G. A novel fluorescent aptasensor based on single-walled carbon nanohorns. Nanoscale. 2011; 3 (11) 4589–4592. [PubMed: 22006211]

Zimmer JP, Kim SW, Ohnishi S, Tanaka E, Frangioni JV, Bawendi MG. Size series of small indium arsenide–zinc selenide core–shell nanocrystals and their application to in vivo imaging. J Am Chem Soc. 2006; 128 (8) 2526–2527. [PubMed: 16492023]

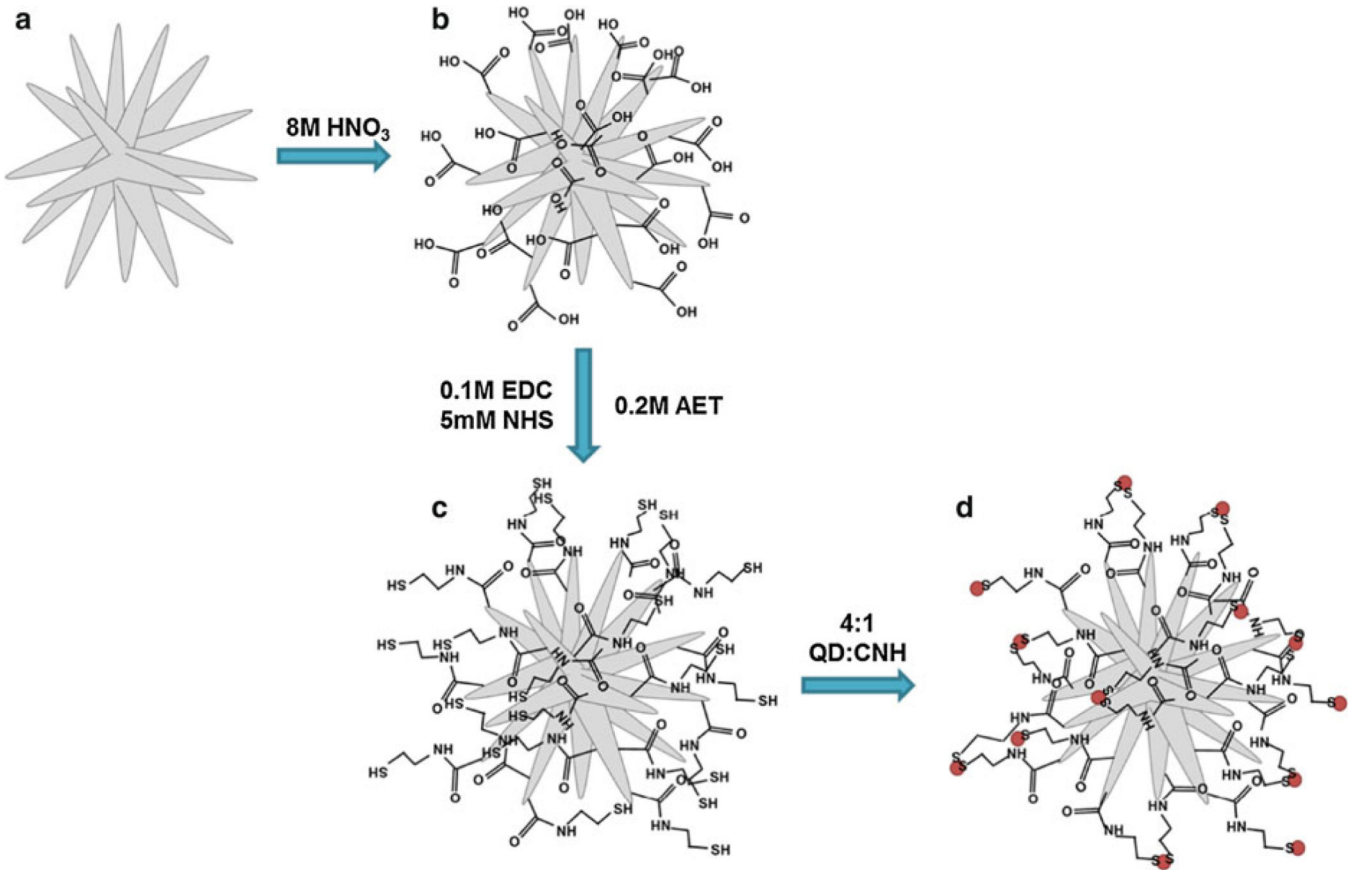

Fig. 1.

Schematic of QD conjugation to SWNH exohedral surface. Pure SWNHs (**a**) were acid oxidized to produce SWNHox (**b**). SWNHox were functionalized with AET using carbodiimide conjugation (**c**) and SWNH–QD complexes (**d**) were synthesized using a ligand interchange approach (QDs denoted by *red dots*). (Color figure online)

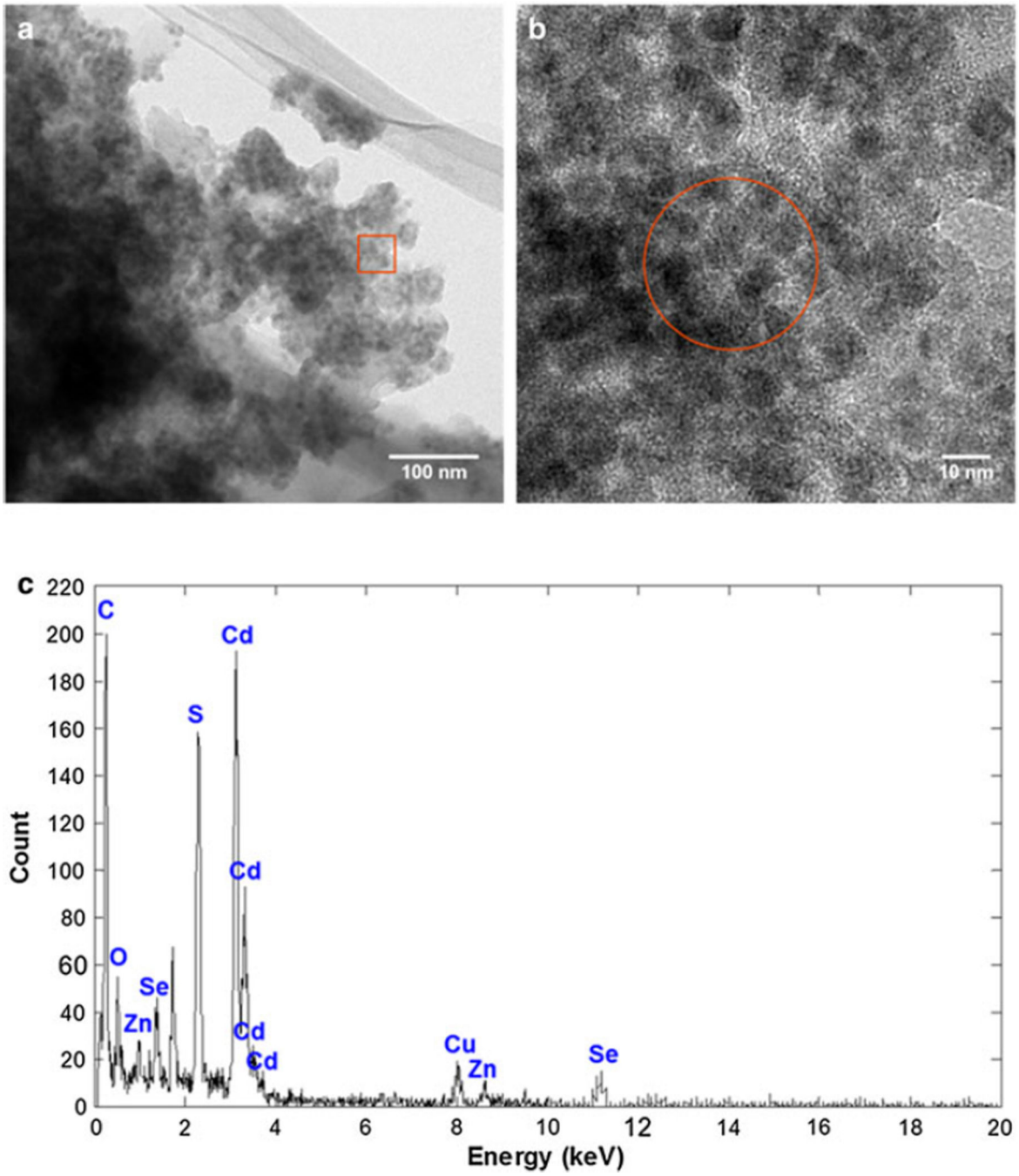

Fig. 2.

SWNHs were successfully labeled with a high density of QDs. **a** TEM micrograph of SWNH–QD conjugates shows highcontrast spherical CdSe/ZnS QDs are attached to the exohedral surface of the lower contrast SWNHs. **b** Higher resolution image of outlined area (*red*) depicted in **a**. **c** EDS spectra of a zone represented by the *red circle* in **b**. (Color figure online)

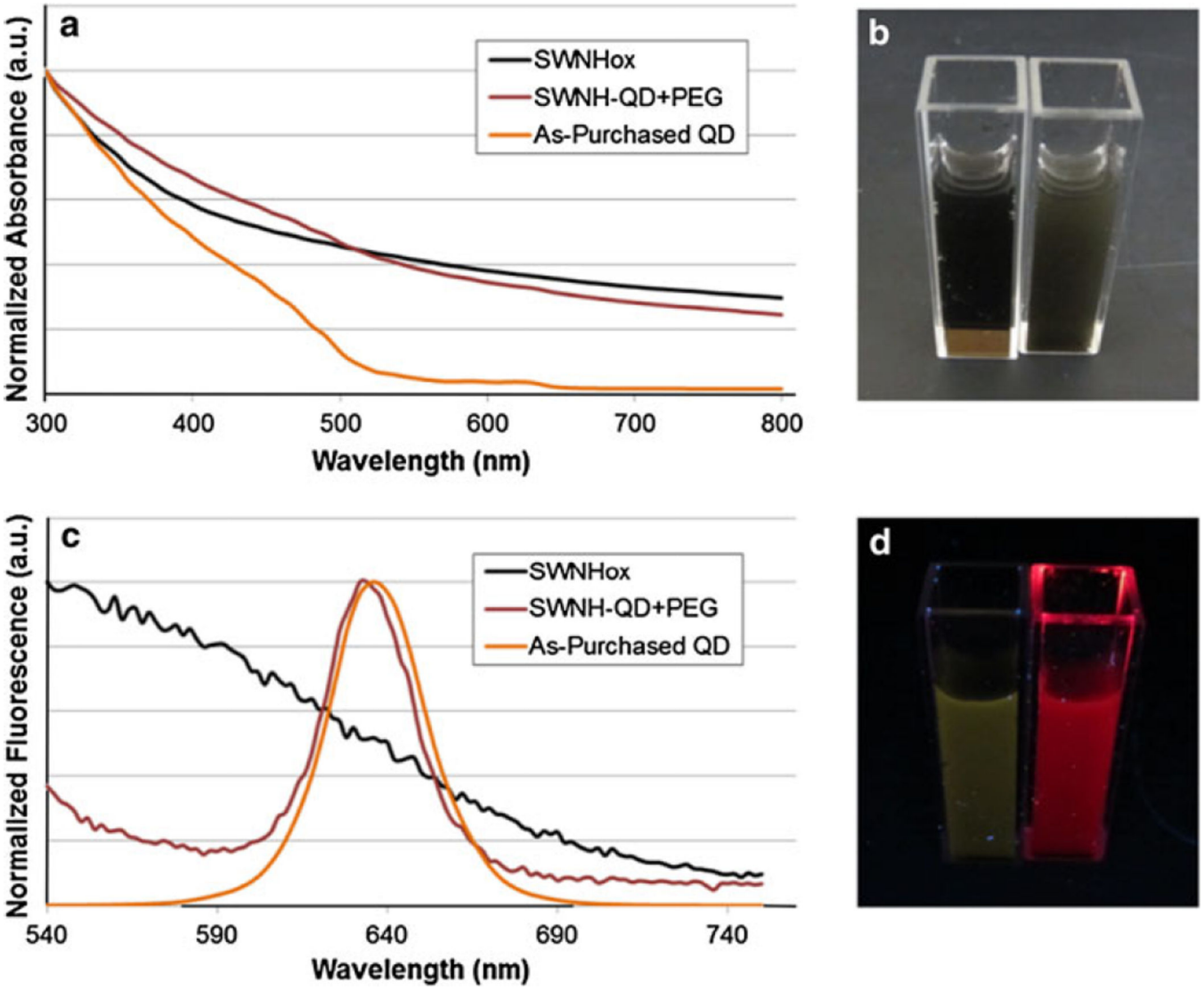

Fig. 3.

a Normalized UV–Vis absorption spectra of SWNHox, SWNH–QD, and as-purchased QDs. **c** Normalized fluorescence spectra of SWNHox, SWNH–QD, and as-purchased QDs excited at 488 nm. **b**, **d** Photographs of SWNHox (vial on *left*) and SWNH–QD (vial on *right*) in solution under **b** fluorescent bulb and **d** UV excitation

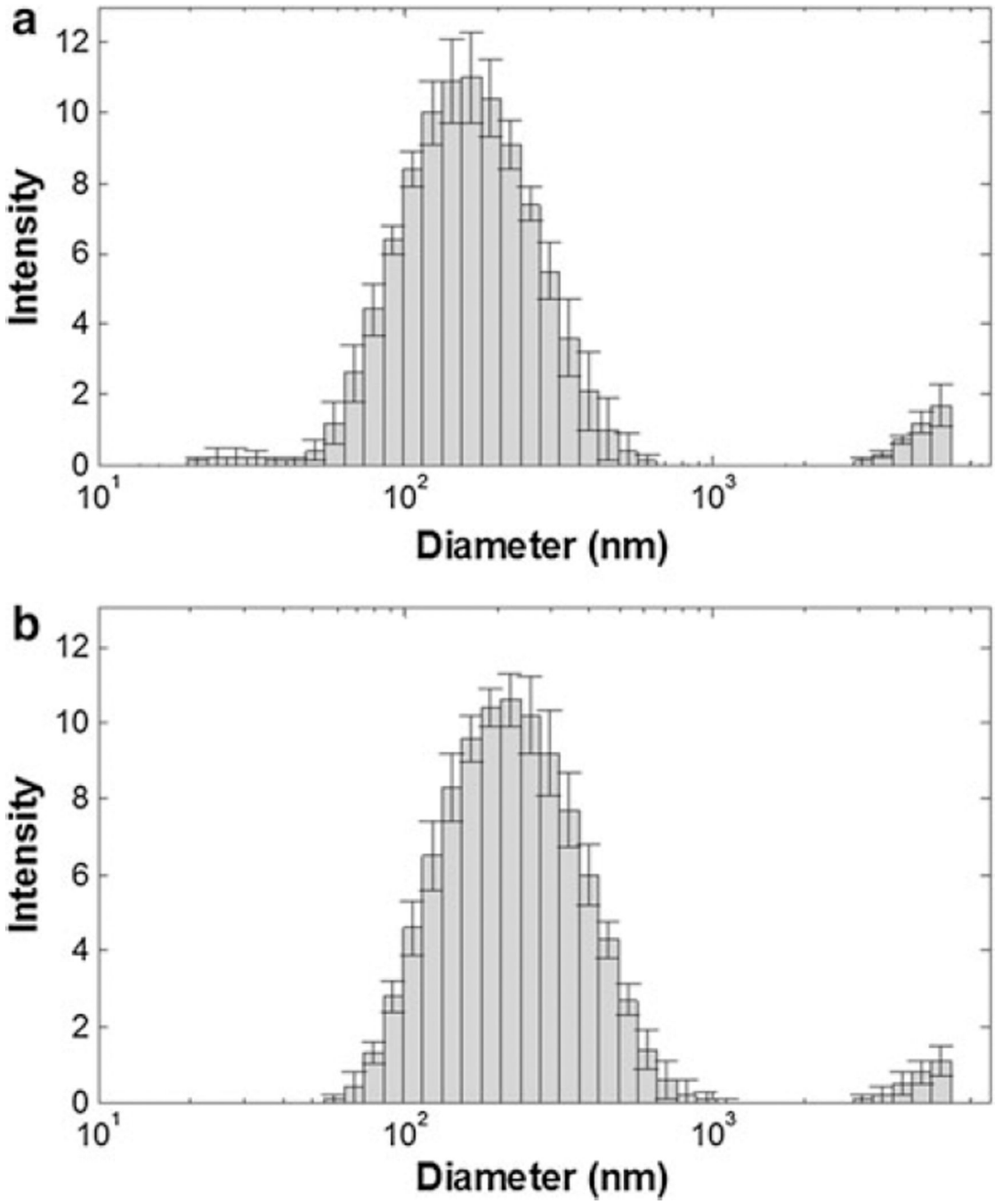

Fig. 4.

Dynamic light scattering of **a** SWNHox and **b** SWNH–QD shows an increase in diameter after QD attachment

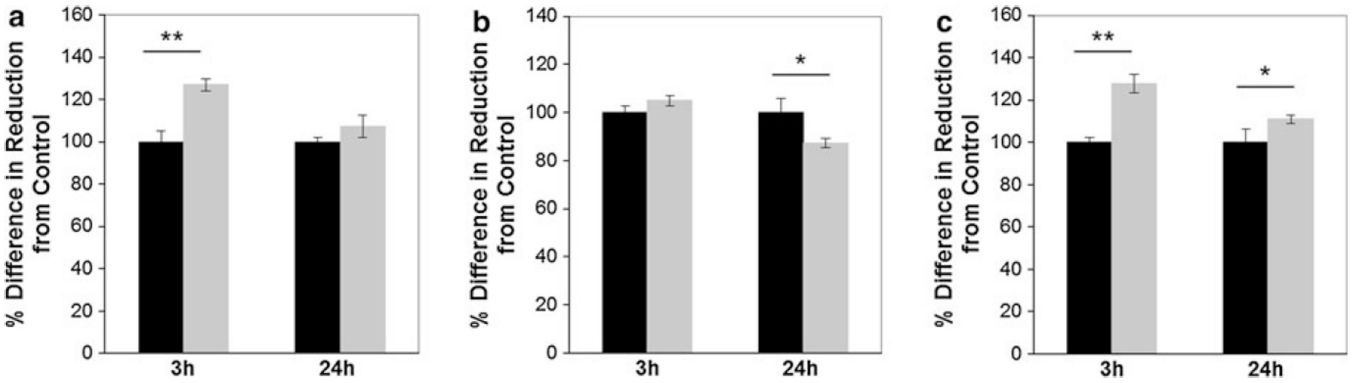

Fig. 5.

SWNH–QD have minimal reduction in metabolic toxicity after 3- and 24-h incubation at 37 °C evaluated with alamarBlue® assay ($n = 3$) in **a** AY-27, **b** MDA-MB-231, and **c** U-87 MG cell lines. *Black bars* represent the untreated control group while *gray bars* represent cells treated with 0.025 mg/mL SWNH–QD. Data represented as percent differences from the control (no nanoparticle) group determined by Eq. S1 in SI. *Denotes statistical difference from the control for $p<0.05$ and **denotes statistical difference for $p<0.01$ using Student's t test

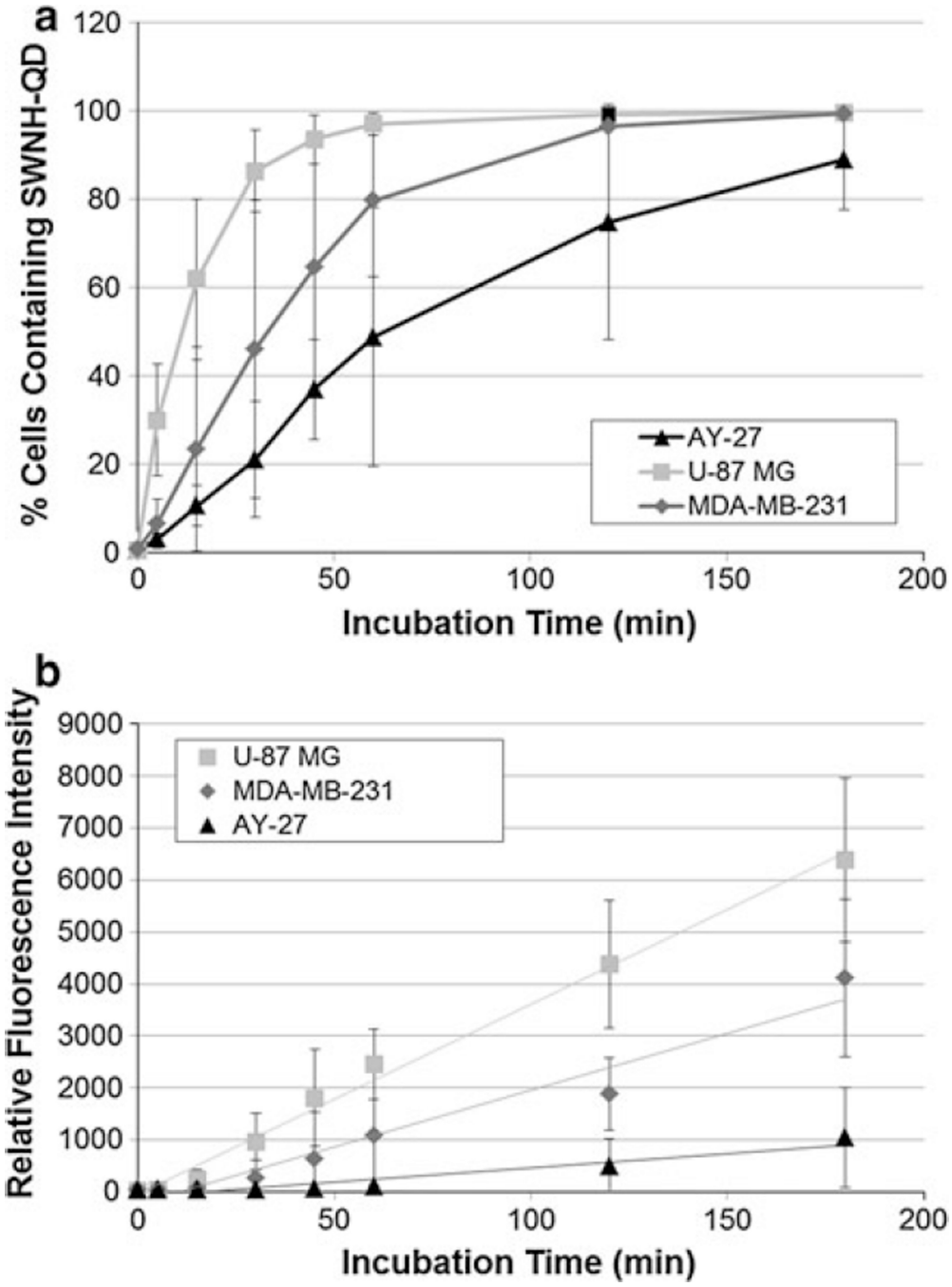

Fig. 6.

FACS results of AY-27, MDA-MB-231, and U-87 MG cells incubated with 0.025 mg/mL SWNH–QDs over time represented as **a** the percentage of cells containing SWNH–QDs in the population measured and **b** median fluorescence intensity of the cell population

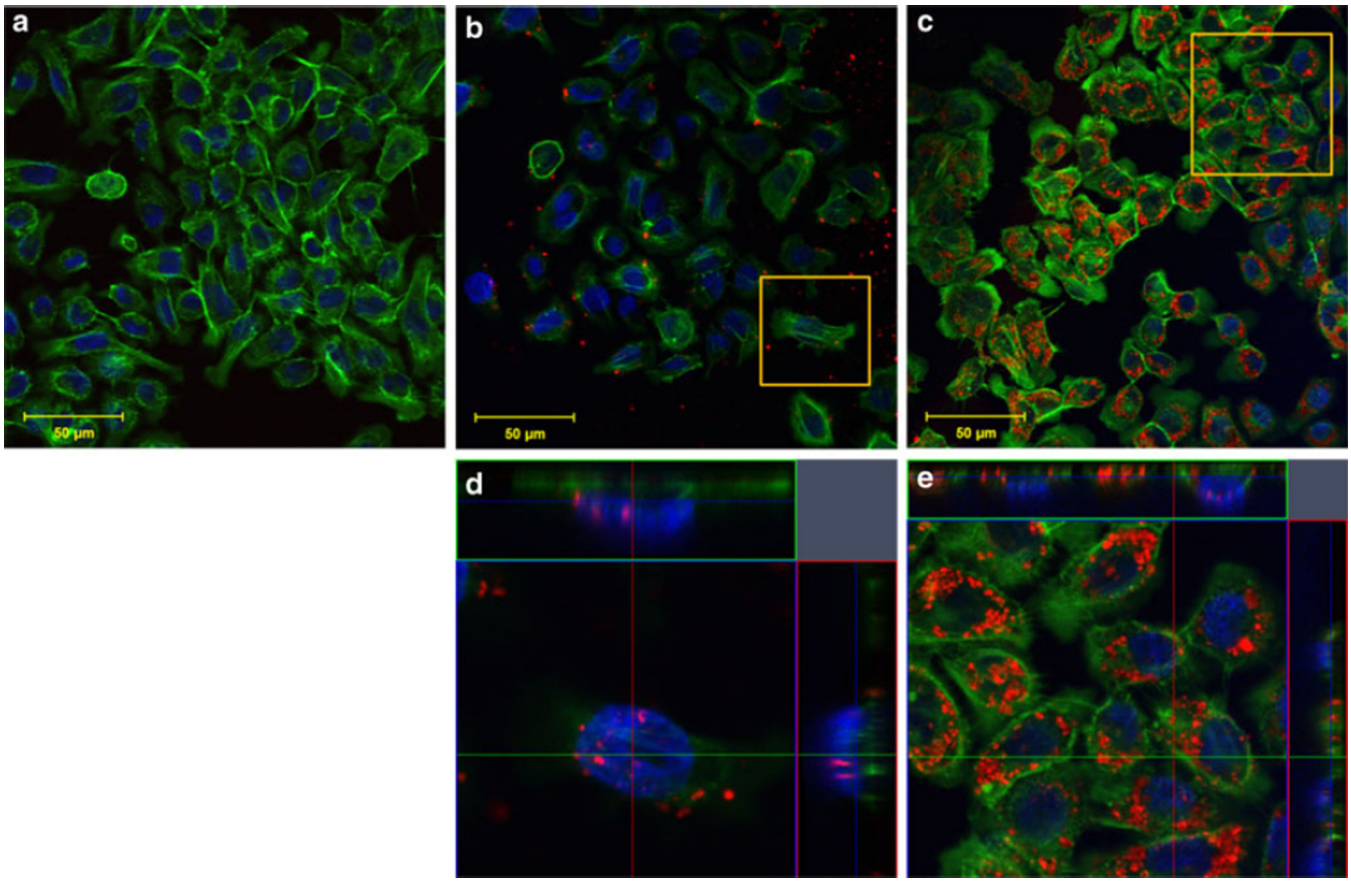

Fig. 7.

AY-27 cellular uptake and binding after **a** 0-min, **b** 60-min, and **c** 24-h incubation with SWNH–QD complexes. **d**, **e** Orthogonal snapshots of the regions of interest in **b** and **c**, respectively. The cross sections in the orthogonal images indicate SWNH–QDs within the nucleus and within the cytoplasm. Staining represented as *green* Oregon Green® phalloidin F-actin stain; *blue* DAPI nuclear stain; and *red* SWNH–QD conjugates. (Color figure online)

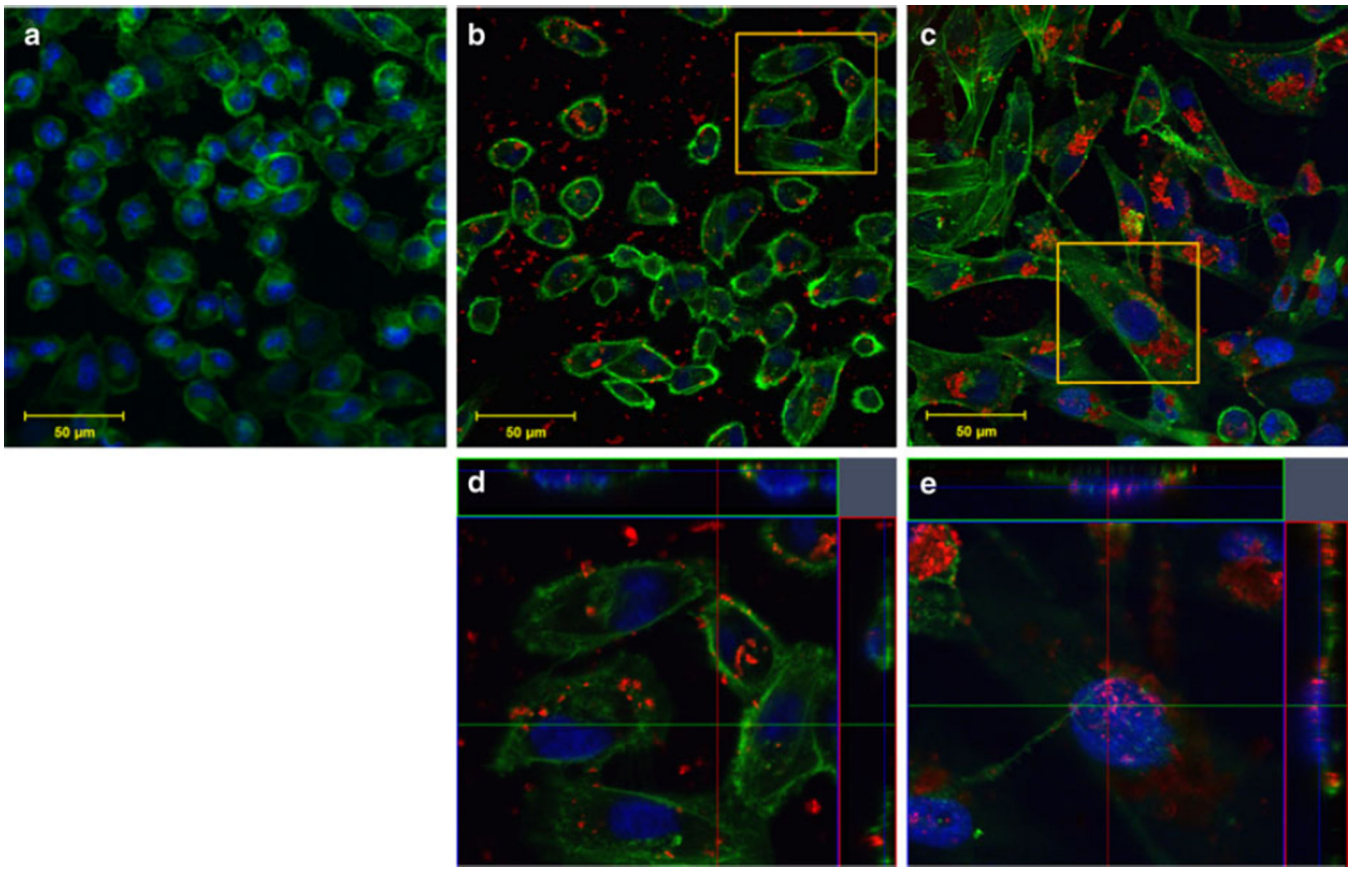

Fig. 8.

MDA-MB-231 cellular uptake and binding after **a** 0-min, **b** 60-min, and **c** 24-h incubation with SWNH–QD complexes. **d**, **e** Orthogonal snapshots of the regions of interest in **b** and **c**, respectively. The cross sections in the orthogonal images indicate SWNH–QDs within the nucleus and within the cytoplasm. Staining represented as: *green* Oregon Green® phalloidin F-actin stain; *blue* DAPI nuclear stain; and *red* SWNH–QD conjugates. (Color figure online)

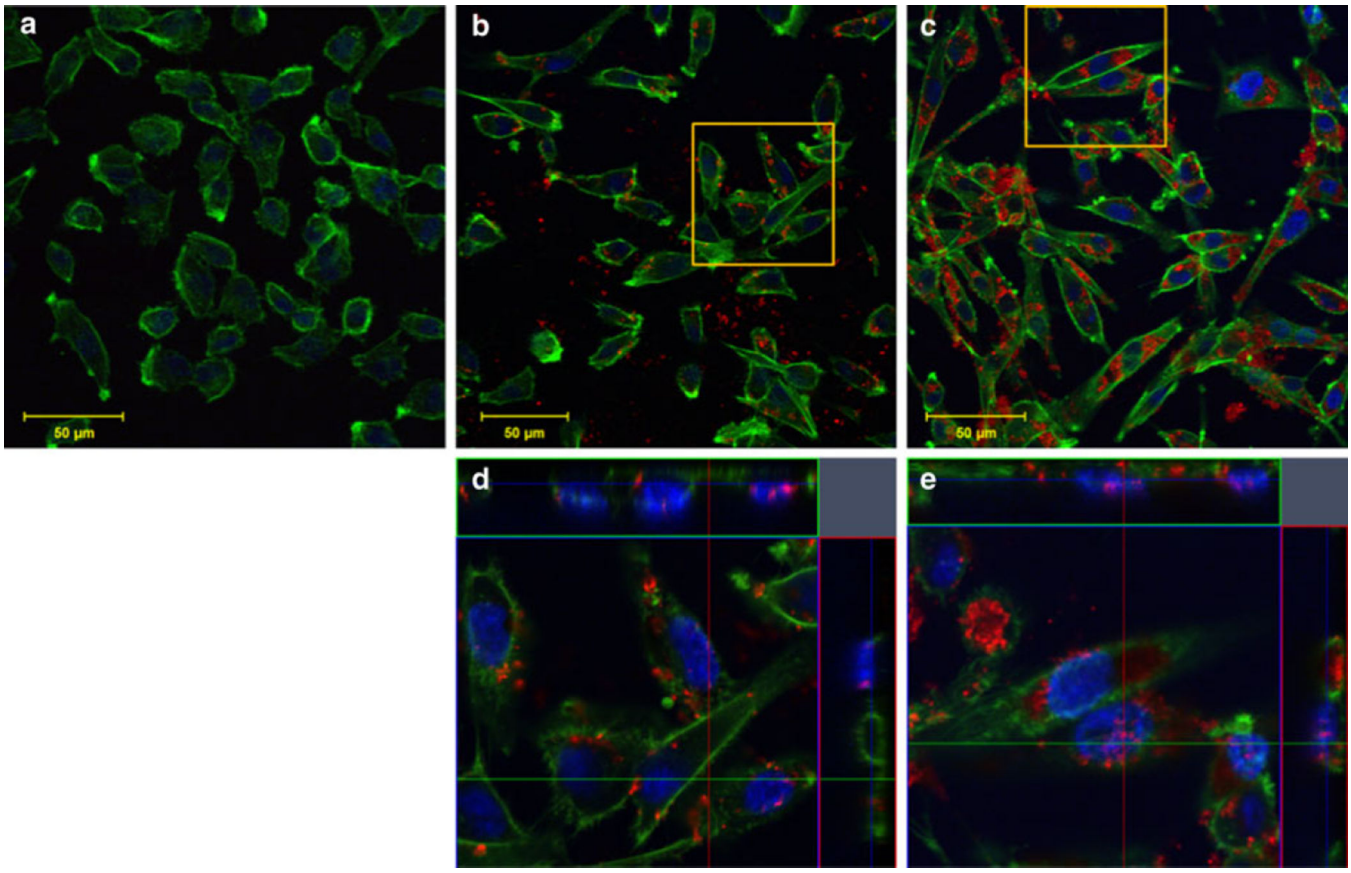

Fig. 9.

U-87 MG cellular uptake and binding after **a** 0-min, **b** 60-min, and **c** 24-h incubation with SWNH–QD complexes. **d**, **e** Orthogonal snapshots of the regions of interest in **b** and **c**, respectively. The cross sections in the orthogonal images indicate SWNH–QDs within the nucleus and within the cytoplasm. Staining represented as: *green* Oregon Green® phalloidin F-actin stain; *blue* DAPI nuclear stain; and *red* SWNH–QD conjugates. (Color figure online)

Table 1

Summary of DLS and ELS results for SWNHox and SWNH–QD

Samples	*Z*-average hydrodynamic diameter (Z_{avg}, nm)	Zeta potential (mV)
SWNHox	150.2 ± 2.7	−51.2 ± 1.8
SWNH–QD	207.5 ± 3.6	−32.3 ± 0.7